Laser speckle imaging of flowing blood

A numerical study

Van As, Kevin; Boterman, Jorne; Kleijn, Chris R.; Kenjeres, Sasa; Bhattacharya, Nandini

DOI
10.1103/PhysRevE.100.033317

Publication date
2019

Document Version
Final published version

Published in
Physical Review E

Editors' Suggestion

Laser speckle imaging of flowing blood: A numerical study

Kevin van As,[1,2,*] Jorne Boterman,[1] Chris R. Kleijn,[1,2] Sasa Kenjeres,[1,2] and Nandini Bhattacharya[3,†]
[1]*Delft University of Technology, Faculty of Applied Sciences, Dept. of Chemical Engineering, 2629 HZ Delft, The Netherlands*
[2]*JM Burgerscentrum for Fluid Mechanics, 2628 CD Delft, The Netherlands*
[3]*Delft University of Technology, Faculty of Applied Sciences, Dept. of Imaging Physics, 2628 CJ Delft, The Netherlands*

(Received 20 May 2019; published 26 September 2019)

Laser speckle imaging (LSI) can be used to study dynamic processes in turbid media, such as blood flow. However, it is presently still challenging to obtain meaningful quantitative information from speckle, mainly because speckle is the interferometric summation of multiply scattered light. Consequently, speckle represents a convolution of the local dynamics of the medium. In this paper, we present a computational model for simulating the LSI process, which we aim to use for improving our understanding of the underlying physics. Thereby reliable methods for extracting meaningful information from speckle can be developed. To validate our code, we apply it to a case study resembling blood flow: a cylindrical fluid flow geometry seeded with small spherical particles and modulated with a heartbeat signal. From the simulated speckle pattern, we successfully retrieve the main frequency modes of the original heartbeat signal. By comparing Poiseuille flow to plug flow, we show that speckle boiling causes a small amount of uniform spectral noise. Our results indicate that our computational model is capable of simulating LSI and will therefore be useful in future studies for further developing LSI as a quantitative imaging tool.

DOI: 10.1103/PhysRevE.100.033317

I. INTRODUCTION

Using diffuse optics for studying dynamics in disordered media is slowly becoming the main enabler of noninvasive optical diagnostic devices [1], finding many applications in the study of biological tissue. These developments are also driven by the increasing demand for readily accessible health care to the rising world population. The main phenomena occurring when light propagates in tissue are absorption and scattering. Absorption of light is used for identifying the different molecular species present in a sample and for determining their concentration. Light scattering, on the other hand, provides information about scatterer size and motion in the sample. In most cases, light is used to illuminate tissue, after which the scattered light is collected in either reflection or transmission.

Illuminating diffuse media with coherent light leads to a random interference pattern called speckle. The speckle is formed by the constructive and destructive interference resulting from path length variations of the light coming to the detector due to surface irregularities or different depths traversed in the media. To interpret such speckle images, physical models of light-tissue interaction are needed. Many different models have been used to study light propagation in tissue with the aim of gaining better insight into the underlying physics and quantifying the detected signals. These techniques range from approximating the light transport as a diffusive process [2–6], to simulating a photon random walk using Monte Carlo techniques [7–9], to modeling scattering from blood using the Mie-Percus-Yevick equations [10].

Any motion of, or inside, the sample causes the speckle pattern to change. The entire pattern could move ("translating speckle"), maintaining speckle correlation, or the speckles could randomly appear or disappear ("speckle boiling") due to relative motion of the scatterers [11]. Since the speckle pattern contains information about the dynamics of the scatterers, speckle imaging is thus used in many applications, ranging from nondestructive testing, stellar interferometry [12], to study of coatings [13,14], to biomedical applications [15]. Therefore, using speckle decorrelation is very attractive for the study of flow behind turbid media, as is the case for many biological applications.

For the specific case of blood flow embedded in tissue, the reflection, absorption, and transmission properties of the different layers that the light travels through each have an impact on the detected light. The standardization of parameters required for medical applications is very challenging, considering that properties of skin and tissue could vary from patient to patient, e.g., depending upon health, age, and ethnicity of the subject. Although there is large variation in optical properties of the static scatterers contributing to the detected signal, the temporal dynamics of the flow or the moving scatterers is also imprinted in the temporal evolution of the speckle patterns. Thus underlying flow can be studied by observing the temporal statistics of speckle fluctuations [16,17]. Using speckle patterns to study any phenomenon has the advantage that no direct imaging is necessary, which largely simplifies the required equipment. *In vivo* blood flow monitoring has been studied quite extensively using speckle-based techniques. These techniques, such as laser speckle contrast imaging (LSCI) and complementary techniques like

*K.vanAs@tudelft.nl
†N.Bhattacharya@tudelft.nl

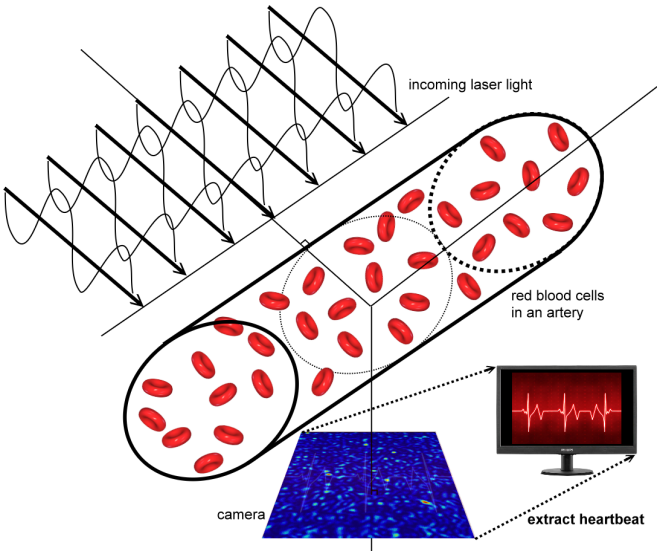

FIG. 1. Sketch of laser speckle imaging applied to an artery: a plane wave of coherent light enters the medium, multiply scatters on the particles, and is finally gathered at a camera set at a 90° angle w.r.t. the incoming light. The result is a noiselike interferometric pattern, known as a speckle pattern, from which we wish to obtain quantitative information.

multiexposure LSCI, along with relevant applications, have been described in detail in a recent review [18].

However, there presently is no agreement in the literature as to how to quantitatively deduce the material's dynamics from the speckle dynamics [19]. One metric for quantifying the speckle dynamics is the speckle contrast, which is the ratio of the intensity's standard deviation and its mean. Since the speckles are dynamic, they will blur when observed with a regular camera due to its finite exposure time, T. The speckle contrast of the blurred speckles depends on T and on the speckle decorrelation time, τ_c. It is widely accepted that τ_c is inversely proportional to the local velocity of the scatterers, but there is disagreement on the proportionality constant [19]. It was even shown theoretically that the velocity distribution affects how C depends on τ_c [20]. Therefore, in order to further develop laser speckle imaging (LSI) as a quantitative measurement technique, a thorough understanding of the scattering process must be acquired.

This can be achieved by using computer simulations, which have the major advantage that noise factors—which are always present in experiments—can be turned off one-by-one to quantify their effect. Therefore, we have developed an interferometric computational model which can simulate the LSI process: an incoming coherent plane wave is multiply scattered by an ensemble of randomly distributed particles—which represent red blood cells in the present study—and is finally collected at a camera (see Fig. 1). The optics code is based on coherent Mie scattering with multiple scattering implemented iteratively but simplified in order to make studying the temporal dynamics computationally feasible. The particles are evolved using an existing computational fluid dynamics (CFD) code, which we have coupled to our optics code. The result is a modular code capable of simulating every aspect of the LSI process. Finally, note that the standard approach for simulating light scattering in turbid media is to use Monte Carlo techniques [7–9], in which light scattering is simulated as random walks of photons. Our approach explicitly tracks the position of each particle, allowing for accurately computing interference effects, and should thus lead to more realistic results.

As a first step towards quantitative LSI, and to validate our simulations, we mimic an experimental setup [21] which used a cylindrical phantom with a size characteristic to that of the external carotid artery (radius ∼1 mm). Spherical particles the size of red blood cells (radius ∼4 μm) were used as scatterers. The flow was given a mean velocity typical to blood in the external carotid artery (∼1 m/s), modulated with a realistic heartbeat. We study the effect of a realistic flow profile by comparing it with plug flow. Using our code, we have simulated the resulting dynamic speckle images of the moving particles. Finally, we have retrieved the frequency spectrum of the modulated heartbeat from the speckles, which also compares well with that from the experimental setup. These results show the capability of our code to simulate the LSI process. In future work, we aim to include the effect of more parameters to develop a quantitative understanding of their influence on speckle dynamics (e.g., the effect of a surrounding static scattering medium: skin and tissue).

II. APPROACH

In this section, we first outline the principle of LSI. Then we elaborate on the underlying electromagnetic theory (i.e., Mie theory) on which our code is based. We proceed by discussing the geometry and the fluid dynamics of our simple case study. Finally, we discuss some relevant notes for obtaining accurate simulation results.

A. Speckle imaging

When phase-coherent light scatters on a surface that is rough at optically relevant scales, a speckle pattern is formed. This is the result of a random interferometric summation caused by the different path lengths the light has traveled as it originates from different spots of the scattering surface. One metric that can be used to extract information from speckle is the speckle contrast [22,23]:

$$C \equiv \frac{\sigma_I}{\langle I \rangle}, \tag{1}$$

where $\langle I \rangle$ is the mean intensity and σ_I is its standard deviation. We speak of fully developed speckle when the phases become uniformly distributed over $[0, 2\pi]$ radians after diffusing or scattering (i.e., no specular component remains) [24]. Then the intensity becomes Gaussian-distributed [25]: $\sigma_I = \langle I \rangle$, and thus $C = 1$. However, when the light depolarizes due to multiple scattering, a value below one may be expected [26].

When both the illumination and the scatterers remain the same, the speckles will also remain unchanged. When the scatterers move without relative motion, the speckles will simply translate at the same rate. However, if there is relative motion between the scatterers, the path-length differences will change, which causes speckles to randomly appear and disappear. This is called "speckle boiling" [11,27], which is a source of noise in laser speckle imaging.

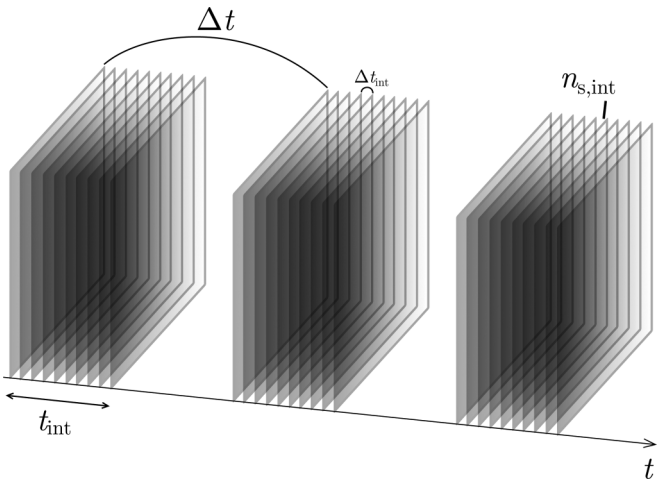

FIG. 2. We sample instantaneous data rapidly (interval Δt_{int}) to mimic a real camera and at distant intervals (Δt apart) to gather temporal data.

Provided that the effect of speckle boiling is sufficiently small, we can use translating speckle to study the collective dynamics of the scatterers [22,28], although nontranslational speckle could also be used [11]. When translating speckle is imaged with a camera, a blurred speckle image will be measured due to the finite camera exposure or integration time. Since blurring decreases σ_I, but does not affect $\langle I \rangle$, the result is a lower C. Therefore, through the camera integration time, the speckle contrast depends on the amount of blurring and thus also on velocity [19]. Our research group has applied this principle previously to experimentally study pulsatile flow in a patient-specific carotid artery [21,29].

In the present work, we introduce a code capable of simulating the whole laser speckle imaging process. The code propagates a coherent plane wave to all scatterers, computes how the light diffracts of each of them, and then propagates all scattered waves to a simulated camera. The resulting image is an interferometric scattering pattern: a speckle pattern. In addition to scattering directly to the camera (i.e., single scattering), multiple scattering is implemented iteratively (see Sec. III B). A separate fluid dynamics code is used for computing the motion of the scatterers, after which the optics code is used to calculate the instantaneous scattering. We mimic the aforementioned blurring effect of a real camera by time-averaging many independent instantaneous simulations in rapid succession with time step Δt_{int}, as can be seen in Fig. 2. This is accurate provided that $n_{\text{s,int}}$ is sufficiently large. We then repeat this process Δt later to obtain temporal data: $C(t)$.

B. Mie theory

For simulating the electromagnetic scattering of light by the scatterers, our code makes use of Mie theory, which describes the scattering of a plane wave by a single sphere [30–33]. The electric field must satisfy the vector wave equation, $\nabla^2 \vec{E} + k^2 \vec{E} = \vec{0}$, where k is the wave number. [The same applies to the magnetic field ($\vec{H}$), but we will leave $\vec{H}$ out of the discussion, because it can always be derived from $\vec{E}$ by taking the curl: $i\omega\mu\vec{H} = \nabla \times \vec{E}$, where ω is the wave frequency and μ is the magnetic permeability.] A complete set of orthogonal basis functions that solve the vector wave equation are the vector spherical harmonics: $\vec{N}_{pmn}$ and $\vec{M}_{pmn}$. Given an incident field traveling in the z direction and polarized in the x direction, $\vec{E}_i = E_0 e^{ikz}\hat{x}$, the scattered field can be expanded in terms of the vector spherical harmonics:

$$\vec{E}_s(\vec{r}) = \sum_{n=1}^{\infty} E_n \left[i a_n \vec{N}^{(3)}_{e1n}(\vec{r}) - b_n \vec{M}^{(3)}_{o1n}(\vec{r}) \right], \tag{2}$$

where $E_n = E_0 i^n (2n+1)/n(n+1)$ is just a prefactor, $\vec{r}$ denotes that the functions depend on position, the superscript "(3)" denotes the usage of the spherical Bessel function of the third kind, and a_n and b_n are the Mie scattering coefficients. μ can be neglected, as its influence is minor for most media: $\mu_{\text{sphere}} \approx \mu_{\text{surroundings}} \approx \mu_0$.

When a far-field approximation is made, the infinite sum in Eq. (2) reduces to a single term, and the scattered field becomes an outgoing spherical wave:

$$\begin{bmatrix} E_{s\parallel} \\ E_{s\perp} \end{bmatrix} = \frac{e^{ik(r-z)}}{-ikr} \begin{bmatrix} S_2 & 0 \\ 0 & S_1 \end{bmatrix} \begin{bmatrix} E_{i\parallel} \\ E_{i\perp} \end{bmatrix}, \tag{3}$$

where $E_\parallel$ and $E_\perp$ are the component parallel and orthogonal to the scattering plane, respectively, $[S]$ is the amplitude scattering matrix which for spherical particles depends only on the scattering angle θ_S and properties of the spherical particle, and r is the radial coordinate (i.e., the distance from the scatterer).

C. Fluid dynamics

In the present work, we use a simple time-dependent flow in a cylindrical geometry:

$$u(r,t) = v(r)F(t), \tag{4}$$

where u is the axial velocity, $v(r)$ is the radial velocity profile, and $F(t)$ is a unitless temporal modulation with a mean of 1.

To study an actual heartbeat, $F(t)$ will be read from a lookup table which contains the shape of a realistic heartbeat, with the same peak-to-peak amplitude (0.75) as in Baker *et al.* [34]. For the simpler sinusoidal case, we take $F(t) = A\sin(2\pi f t) + 1$, with $2A = 0.75$. The particle positions are integrated in time using the Euler forward scheme with dimensionless time step $\Delta t^* = f\Delta t = 5 \times 10^{-4}$, which yields a maximum relative discretization error of 0.1%.

The exact solution for the radial velocity profile in a cylinder is Hagen-Poiseuille flow,

$$v(r) = 2\langle v \rangle \left[1 - \left(\frac{r}{R} \right)^2 \right], \tag{5}$$

where $\langle v \rangle$ is the mean velocity, and R is the radius of the cylinder. For this realistic flow profile, there will be relative motion between the scatterers and there will therefore be speckle boiling. To investigate its influence, we will compare the results with plug flow: $v(r) = \langle v \rangle$.

D. Data analysis

To extract useful information from our simulated speckle images, three factors in particular are important: speckle

boiling causes temporal noise, the camera should be sufficiently big with a sufficient resolution, and for a large camera the speckle contrast should be calculated using windowing.

First, speckle boiling is a physical noise factor caused by the relative motion of the scatterers [11], such as is the case in a fluid. In this work, we will study flow with and without speckle boiling, as was discussed in the previous section, which enables us to determine its influence.

Second, to mitigate statistical noise, a sufficient number of speckles must be captured, and a sufficient number of pixels should be used to represent each speckle (i.e., resolution). The first ensures that the speckle space is well represented and thus that the data samples are uncorrelated; the latter ensures that speckles are not smoothed over the finite area of a pixel, because that artificially reduces the measured C which needs to be corrected [35,36]. For a real camera of 1024^2 pixels, it was found that about 4^2 pixels per speckle suffices for obtaining a good result [36,37]. For our simulated camera, however, we are realistically limited to about 256^2 pixels by computational constraints.[38] Using 256^2 pixels with 4^2 pixels per speckle, we obtained a noise signal for C, which indicates bad statistics.

To overcome this, we instead have our simulated camera underresolve the speckles, typically using merely $(1/5)^2$ pixels for each speckle in this paper. One cannot do this with a real camera, as this would artificially reduce C, because of spatial averaging over the finite pixel size. However, our simulated pixels are infinitesimal points in space. Thus the underresolving in our simulations is equivalent to using infinitesimal pixels whose separation is much greater than the typical speckle size, as is recommended by Skipetrov *et al.* [35]. In that manner, the simulated camera effectively samples an area $400\times$ larger than it could possibly have for resolved speckle. Therefore, by underresolving the speckles, we retain all intensity fluctuations, while increasing our statistical sample size.

Third, since the amplitude scattering matrix of a sphere in Eq. (3) depends on the scattering angle, $\langle I\rangle$ will generally not be constant across an image, which artificially increases σ_I. Therefore, applying Eq. (1) directly will give a larger value for C than it should have been. This is especially true for a large camera, such as our simulated camera. If the system is sufficiently dense (i.e., high particle concentration), singly scattered light will be negligible compared to multiply scattered light. For multiply scattered light, the light is incident from random directions, resulting in a randomly distributed θ_s and thereby averaging out the effect of $[S](\theta_s)$.

However, for relatively dilute experiments, such as studied in our simulations due to computational constraints, single scattering contributes significantly. To overcome the issue at hand, we use local speckle contrast analysis [39], in which C is calculated through windowing, and then averaged to obtain the (average) speckle contrast of the whole image:

$$C = \frac{1}{M_x M_y}\sum_{x=0}^{M_x-1}\sum_{y=0}^{M_y-1} C_{x,y}. \tag{6}$$

We will discuss the required window size in Sec. IV A.

III. CODE DESCRIPTION

Our code comprises three parts: first computational fluid dynamics (CFD) is used to evolve the particles in time, then the particle positions are extracted from the fluid simulation and processed to be used as the input for the optics code, and last a Mie-based optics code is used to compute the scattering of an incoming plane wave by the collection of particles.

A. Computational fluid dynamics (CFD)

To obtain the flow field and particle movements, one can readily apply CFD, in which the discretized Navier-Stokes equations describing fluid momentum and mass conservation are solved numerically. Particles are typically simulated using Lagrangian particle tracking. However, since the flow considered in this paper is rather simple, we use the exact solution of the Navier-Stokes equations for the velocity of the particles instead (see Sec. II C). When a particle leaves the cylinder, it is teleported back to the entrance at the same radial and polar position (i.e., cyclic boundary conditions).

Regardless, our code is designed to be compatible with any existing CFD code (e.g., OpenFOAM). This is possible because the speed of light is very large. Therefore, the particles cannot move a fraction of λ in the time δt it takes the light to scatter off of all particles (i.e., $v\delta t \ll \lambda$ results in $v \ll 2\times 10^2$ m/s for the case of our interest, whereas $v \sim 1$ m/s). Consequently, CFD and the optics code are one-way coupled: CFD does not depend on the optics code, but its output serves as the input of the optics code.

B. Optics

Our optics code uses the Mie far-field solution Eq. (3) to compute the scattered light of each particle separately, while explicitly keeping track of the phase. The required Mie scattering coefficients in Eq. (2) are computed using the BHMIE.F90 script from the book of Bohren and Huffman [31], using the cutoff index n_C as was found empirically by Wiscombe [40]. Computing the Mie solution for all of space is very computationally demanding, but luckily it needs only to be evaluated at the points of interest, being the individual points of our virtual camera (i.e., pixels of zero area), and at the positions of every particle for multiple scattering.

Multiple scattering is implemented iteratively. In the first iteration, the incident laser light is scattered via each particle l to each of the $N-1$ other particles $i \neq l$:

$$\vec{E}^0_{il} = \text{scatter}_{l\to i}(\vec{E}_{\text{incident}}), \tag{7}$$

where the "scatter" operation refers to Eq. (3). In successive iterations p, every particle i then has $N-1$ incoming waves from source particles $l \neq i$, which it should scatter to all $N-1$ other particles $j \neq i$:

$$\vec{E}^p_{ji} = \sum_{l\neq i} \vec{E}^p_{jil}, \tag{8}$$

$$\vec{E}^p_{jil} = \text{scatter}_{i\to j}\left(\vec{E}^{p-1}_{il}\right). \tag{9}$$

This process includes backscattering (i.e., $j = l \neq i$). The iterative process is repeated until the maximum of the magnitudes of all scattered electric fields $\vec{E}^p_{ji}$ is a factor 10^8 smaller

than the incident light, which for our simulations results in about six or seven iterations. Subsequently, all (multiply) scattered fields $\vec{E}^p_{ji}$ are scattered to each of the M camera pixels c:

$$\vec{E}_{ci} = \sum_{l\neq i} \text{scatter}_{i\to c}\left(\sum_p \vec{E}^p_{il}\right). \tag{10}$$

Finally, the intensity at each pixel c can be computed:

$$I_c = \left|\sum_i \vec{E}_{ci}\right|^2. \tag{11}$$

The complexity of the resulting algorithm is $N^2(N+M)$, to be repeated for each time step. The code is perfectly parallel (i.e., using x cores is x times faster), because a great number of independent instantaneous simulations are performed.

Through our iterative process, two implicit (and arguably too strong) assumptions and simplifications are made. First and most strongly, we use the Mie far-field solution Eq. (3) at the length scale of the interparticle distance. It is clear that this assumption is easily violated: for particle radius $a = 4$ μm and $\lambda = 600$ nm, the interparticle distance should be $\delta r \gg 0.1$ mm to satisfy the assumption. However, blood has a hematocrit of ∼50%, meaning the typical distance between adjacent red blood cells is of the order of the particle radius. Although this assumption is not satisfied for true blood, it is still satisfied in our simulations for 95% of the interparticle distances ($\langle\delta r\rangle = 3.45$ mm), because we are limited to relatively few particles due to computational constraints. Therefore, this assumption does not affect our results at present. The second assumption is that Mie theory requires an incoming plane wave; therefore, we approximate the outgoing spherical wave Eq. (3) of the first particle as a plane wave at the position of the second particle:

$$\Psi(r) = \frac{e^{ikr}}{kr} \approx \Psi(z) = e^{ikz}\frac{e^{ik\delta r}}{k\delta r}\left(1 - \frac{z}{\delta r}\right). \tag{12}$$

This is a plane wave provided that $a \ll \delta r$, which is much more easily satisfied than the previous assumption.

The scattering matrix must be computed $N^2(N+M)$ times, comprising over 90% of the computational effort of the code. Since we had made a far-field assumption, the scattering matrix depends only on the scattering angle. Therefore, we precompute it with 100 samples per degree, allowing for accurate interpolation, and yielding a speedup of a factor ∼10. In conclusion, despite some assumptions being arguably too simplifying, they enable us to simulate time-dependent laser speckle imaging within a feasible computational effort.

As an alternative to our approach, one could instead use more sophisticated methods such as the T-matrix method. With some adaptations, existing T-matrix codes—such as GMM [41] or FaSTMM [42]—could be implemented within our combined fluids and optics framework by replacing the core calculation routines of our optics code. Using the T-matrix method, the above far-field assumption is eliminated: the calculated multiply scattered field is exact. It would even become possible to study nonspherical particles. However, a single (temporal) simulation of ours requires $O(10^4)$ individual scattering simulations (cf. Fig. 2), which is not computationally feasible without our assumptions. Furthermore, we will argue in the following section that our simulations are already sufficiently accurate for our purposes.

TABLE I. Simulation parameters.

Optics	Refractive index	$n_{\text{sphere}} = 1.52$ $n_{\text{medium}} = 1$
	Wavelength	$\lambda = 532$ nm
Flow system	Fluid mean velocity	$\langle v\rangle = 1$ m/s
	Flow signal frequency	$f_{\text{sinusoidal}} = 1$ Hz $f_{\text{heartbeat}} = 1.20$ Hz
	Particle radius	$a = 4$ μm
	Number of particles	$N = 100$
	Radius cylinder	$R = 1$ mm
	Length cylinder	$L = 1$ cm
Camera	Number of pixels	$M = 128 \times 128$
	Physical size[a]	1.25 cm × 5.0 cm
	Distance from cylinder	25 cm
Simulation	Camera integration time	$\Delta t_{\text{int}} = 100$ μs
	No. integration samples	$n_{\text{s,int}} = 40$
	Total simulation time	$T = 40$ periods
	Data sampling rate	20 samples/period

[a]Note that our simulated camera size is without any lenses.

IV. RESULTS

All simulation parameters are summarized in Table I for reference.

Figure 3 shows several speckle figures. Instantaneous (i.e., no camera integration) speckle is shown in Fig. 3(a). In this figure, the typical speckle is 4 ± 1 by 5 ± 1 pixels in size, which translates to 16 ± 3.9 μm by 78 ± 16 μm. Theoretically, the speckle size should correspond roughly to the characteristic width of the point-spread function (PSF) of the aperture [19]:

$$d_{\text{speckle}} \sim \frac{\lambda z}{D}, \tag{13}$$

where z is the distance between the object and image plane, and D is the aperture diameter. Note that in our simulations the "aperture" is the cylinder's frontal area: 1 cm by 2 mm. Since our aperture has an aspect ratio of 5, the speckles have aspect ratio 1/5. That is why we chose our camera to be rectangular with aspect ratio 4, as to measure (almost) circular speckles. Using the settings in Table I, Eq. (13) results in 13 μm by 67 μm. Especially since we compare only a "characteristic" width, our results correspond well with theory, which validates the interferometric behavior of our code [43].

Figure 3(b) shows the corresponding time-integrated speckle image. For our settings, the speckles blur over ∼10% of the camera's width, in the direction of motion. Note, however, that these resolved speckle figures were created with a 1 mm by 4 mm camera for the sake of visualization, whereas the following results use unresolved speckle (as was discussed in Sec. II D), such as is shown in Fig. 3(c).

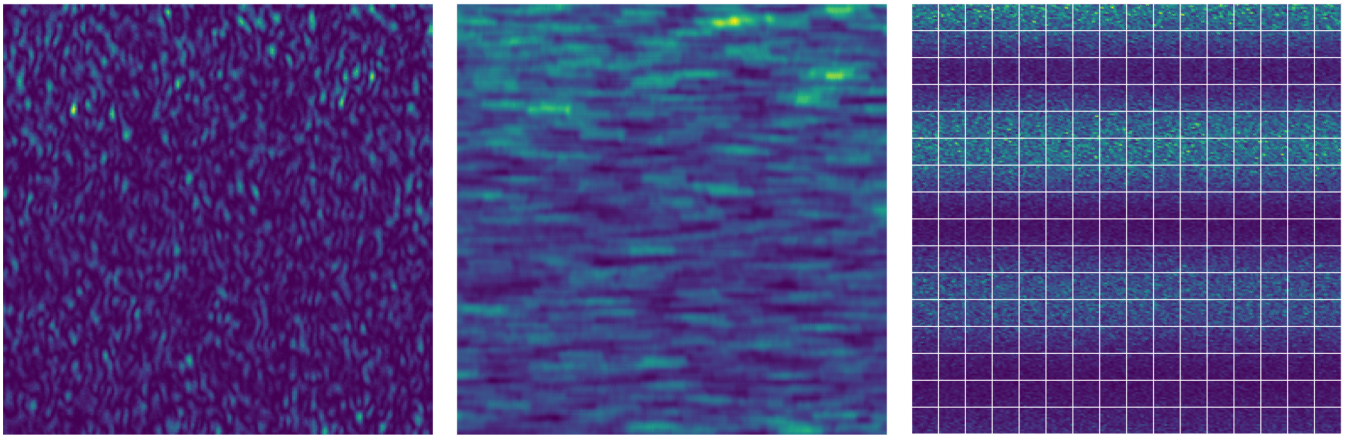

(a) Simulation: resolved, instantaneous (b) Simulation: resolved, blurred (c) Simulation: unresolved, blurred

FIG. 3. A few characteristic speckle figures: the influence of the camera integration time and resolved versus unresolved speckle. (b) The temporally blurred version of panel (a). Note that the color ranges differ: absolute values are meaningless, and the blurred image (b) has a factor 10 lower intensity range than panel (a), which would have caused panel (b) to appear mostly dark blue. The 16 × 16 grid used for local speckle contrast analysis is also shown (c). Deviations from Table I: the camera size in panels (a) and (b) is 1 mm × 4 mm, and all three figures use 256^2 pixels.

A. Convergence

To obtain accurate results, several factors are important, which we will now discuss. First, it is important to have a sufficient number of pixels (M) (i.e., spatial resolution) in combination with a sufficiently large camera (to sample enough of speckle space to obtain statistical significance). Second, a sufficient number of camera integration samples ($n_{\mathrm{s,int}}$) (i.e., temporal resolution) is required to mimic a real camera. Third, an appropriate camera integration time (Δt_{int}) should be used, depending on the characteristic velocity ($\langle v \rangle$). We will not discuss the latter in this paper, other than noting that $\Delta t_{\mathrm{int}} = 100$ µs is appropriate for $\langle v \rangle = 1$ m/s, given that we obtain good results (whereas we have found that either a too large or a too small Δt_{int} results in noise).

Figure 4(a) shows the effect of the number of pixels (M), and the used windowing size [cf. Eq. (6)] on the speckle contrast of an instantaneous simulation. As was discussed in Sec. II A, we can expect $C = 1$ for fully developed speckle, but since we have a minor (∼10%) contribution of multiple scattering, a value slightly below 1.0 can be expected. The figure shows that when no windowing is used, the computed C is significantly too high. The reason for obtaining $C > 1$ is that our camera is sufficiently large for interferometric fringes to be visible [see Fig. 3(c)], the cause of which was discussed in the third point of Sec. II D. The fringes increase σ_I, and thus also C [cf. Eq. (1)]. By using an increasing number of smaller windows, we find that C decreases. This happens because we effectively zoom in on the fringes, leaving only

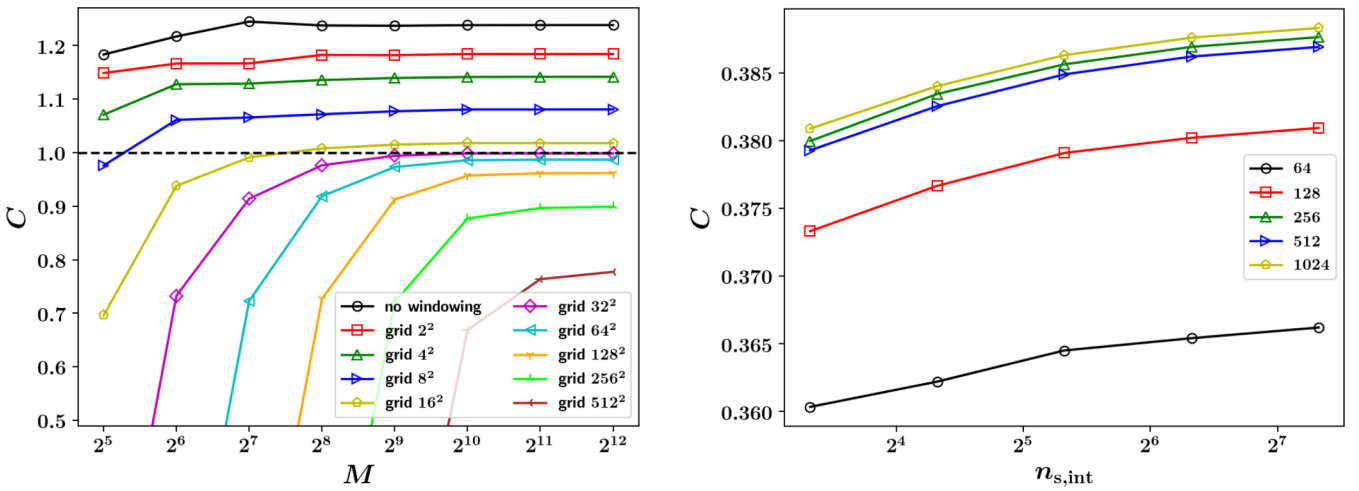

(a) Spatial Convergence (b) Temporal Convergence

FIG. 4. The effect of the spatial (number of pixels, M) and temporal ($n_{\mathrm{s,int}}$) resolution and the effect of windowing on the computed speckle contrast (C). The notation "grid 16^2" denotes subdividing the image in a 16 × 16 grid of calculation windows [i.e., windows of 8^2 pixels for 128^2 (2^7) total pixels], as is illustrated in Fig. 3(c).

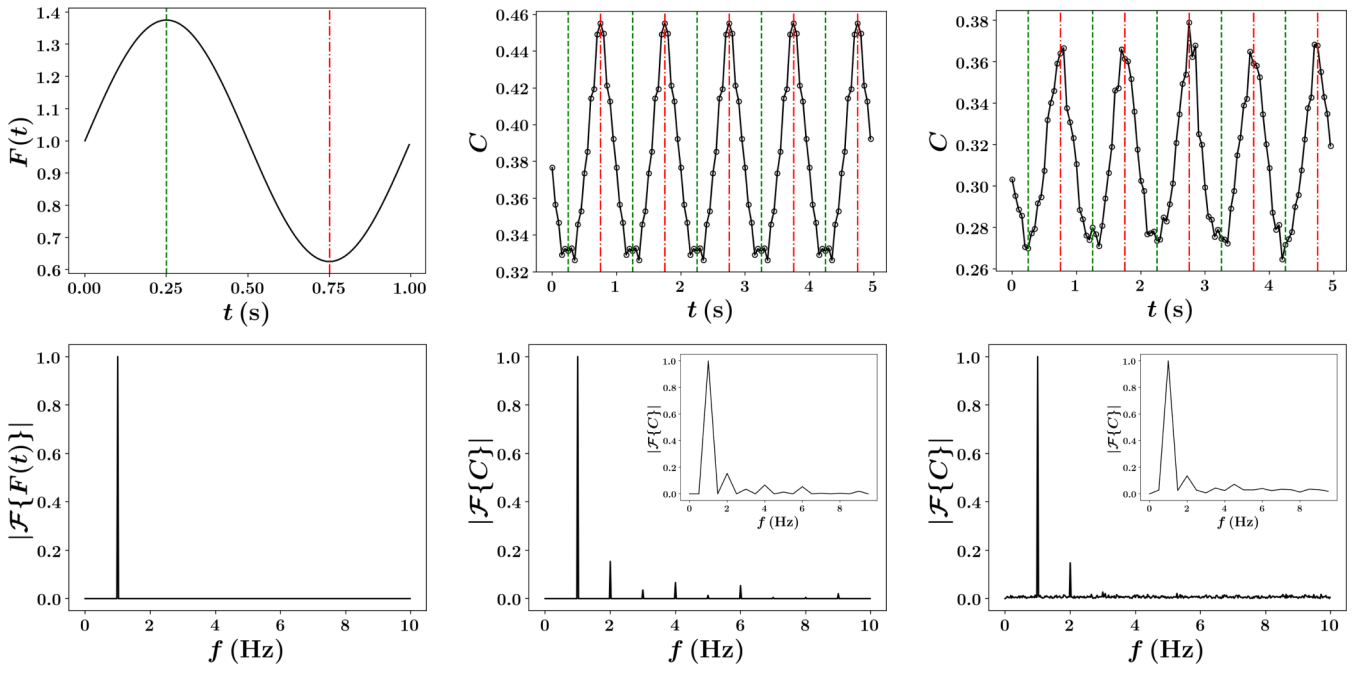

(a) Input (temporal modulation) (b) Plug Flow (c) Poiseuille Flow

FIG. 5. Simulation results for the sinusoidally modulated flow. Top: obtained speckle contrast time series, shown for five simulated periods. Bottom: its frequency spectrum obtained from 40 simulated periods. Insets on bottom: the frequency spectrum as obtained from merely two simulated periods.

the speckles to be seen [see the grid drawn on Fig. 3(c)]. Therefore, windowing with sufficiently small windows is a good thing. This is evidenced by the convergence to a value just below $C = 1.0$, up to "grid 64^2".

However, as we use increasingly small windows for "grid 128^2–512^2," C starts to become increasingly underestimated. The same effect is seen in the bottom-left part of the figure. This happens because we then effectively zoom in on the speckles, which results in a reduced σ_I and therefore a reduced C and will eventually result in $C = 0$ (i.e., in the limit of infinitely small windows). Additionally, the point at which windows become too small is relative to the speckle size, because a sufficient number of speckles should be visible in a window to accurately calculate C. For example, at 4096^2 (2^{12}) pixels, speckles are about 6.4^2 pixels in size; thus using windows of 8^2 pixels (as is the case for "grid 512^2") is clearly too small. The figure shows that this effect begins roughly at "grid 128^2", corresponding to a window-size-to-speckle-size ratio of 5. Therefore, we conclude that this ratio should be larger than ∼5 to obtain quantitative results. Furthermore, all lines are consistently satisfyingly close to their asymptotic value when windows of at least 8^2 pixels are used, which is consistent with the experimental heuristic of using 5^2–7^2 pixels as a compromise between spatial resolution (i.e., small windows) and sufficient statistics (i.e., large windows) [20] to obtain qualitative results.

Consequently, a balance between these two opposing effects is required. The windows corresponding to "grid 64^2" and "grid 32^2" differ by merely ∼1.2%, and "grid 16^2" deviates by merely ∼3.1% from "grid 64^2," which indicates convergence in that middle range. Given the computational constraints, we decided to choose 128^2 (2^7) pixels, for which a 16×16 grid (i.e., 8×8-pixel windows) is most appropriate with a ∼2.6% error w.r.t. its value at 4096^2 (2^{12}) pixels, and ∼0.4% w.r.t. the asymptote of "grid 64^2."

In Fig. 4(b) the effect of the number of camera integration samples ($n_{s,int}$) on C for a temporal simulation can be seen. For the sake of completeness, the result is also shown for a varying number of pixels. The first thing to note is that the convergence behavior is independent of M, indicating that spatial and temporal convergence can be studied independently. The 128^2 pixels case deviates merely ∼1.2% from those with more pixels, indicating that 128^2 pixels are also appropriate for a temporal simulation. For $n_{s,int} = 10$, we have a ∼2% error w.r.t using $n_{s,int} = 160$, which reduces to ∼0.5% for $n_{s,int} = 40$. As a general rule of thumb, we found that one needs a higher $n_{s,int}$ for a smaller camera. For our present camera, $n_{s,int} = 10$ would suffice, but in line with our simulations with a smaller camera, we chose $n_{s,int} = 40$ in the present work as well.

B. Extracting a heartbeat

As was discussed in Sec. II C, we study four distinct cases: sinusoidal plug flow, sinusoidal Poiseuille flow, heartbeat plug flow, and heartbeat Poiseuille flow. Tracer particles suspended in each flow were simulated, after which our LSI code was used to simulate speckle.

Figure 5 shows $C(t)$ and the frequency spectra for the sinusoidal cases. For plug flow [Fig. 5(b)], we obtain a perfectly periodic signal. This happens because we obtain the very same particle positions for successive cycles due to our

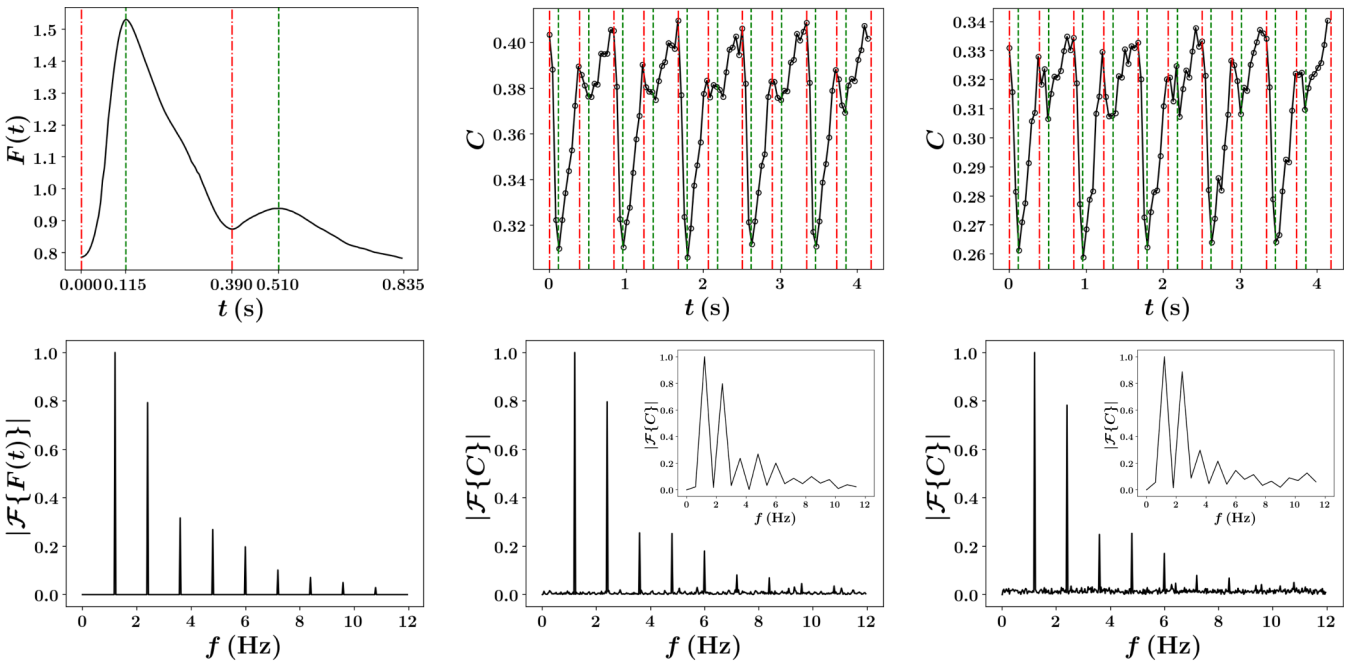

(a) Input (temporal modulation) (b) Plug Flow (c) Poiseuille Flow

FIG. 6. Simulation results, like Fig. 5, but now for a heartbeat-modulated flow.

cyclic boundary conditions. For Poiseuille flow [Fig. 5(c)] on the other hand, we retrieve a periodic signal, with some noise. Most of that noise can be attributed to speckle boiling. In the frequency spectra it can be seen that the main frequency peak of the input signal is easily reconstructed, for plug flow and Poiseuille flow alike. It can be seen that the effect of speckle boiling on the frequency spectrum is minor noise with roughly the same amplitude at all frequencies, which is easy to filter out if we would want to.

Unlike the input signal, the output signal also shows a frequency peak at twice the main frequency. This is caused by the fact that $C(t)$ is broad at its troughs, but narrow at its crests. This widening and narrowing effect can be created by superimposing a cosine of twice the sine's frequency. $C(t)$ shows this behavior, unlike the input signal, because C does not simply scale linearly with velocity (u) [19]. Hence we cannot expect $C(t)$ to be identically proportional to u. More specifically, for low velocities, C drops sharply from 1, whereas for high velocities C approaches the asymptotic value of 0 slowly. Thus changes at a low velocity (troughs of u; crests of C) result in large changes in C, whereas changes at a high velocity (crests of u; troughs of C) result in a smaller change in C. Therefore, the crests of C should theoretically be more narrow than its troughs, as is also observed.

The results for the heartbeat-modulated cases are shown in Fig. 6. Just like for the sinusoidal cases, $C(t)$ shows the same features as the input signal. That is, there is a clear mapping between all local minima and maxima, and crests of u again correspond to troughs of C and vice versa. For plug flow [Fig. 6(b)], the signal is nicely periodic with little noise. In the frequency spectrum it can be seen that the original main frequency is found, and the characteristic higher order frequencies are also retrieved. The relative peak heights are not identical as those of the input signal, but—as was also concluded for the sinusoidal case—they should not be, because C does not scale linearly with u. The little noise that is present is caused by the different particle positions for each cycle, as with a period of 0.835 s the cyclic boundary conditions do not result in identical particle positions in the next cycle, as had been the case for the sinusoidal modulation with a period of precisely 1 s.

For Poiseuille flow [Fig. 6(c)], we once again obtain a signal which is more noisy than plug flow, which may again be fully attributed to the speckle boiling associated with the Poiseuille flow profile. Taking the frequency spectrum of plug flow as a reference, it may be concluded that the effect of speckle boiling is to apply spectral noise independent of frequency, as was also observed for sinusoidal flow. The relative peak heights are within 2% of those of plug flow—so within our convergence errors—proving that speckle boiling has no significant effect on our ability to use LSI for studying the dynamics of a flow system.

Our group has previously applied the principles outlined in this paper to extract the heartbeat in an experimental setup [21]. The heartbeat was also measured *in vivo* using this technique [29]. Our simulations compare well with those experimental results.

C. Future work

The results presented thus far show the capability of our code to simulate LSI. As merely the first step, we have applied our LSI code to extract a heartbeat from a simulated flow and studied the effect of (the noise induced by) speckle boiling. Clearly, simpler techniques such as light-absorption techniques are already able to do this, as only a (qualitative) sensitivity to fluctuations in blood density is required. The

real power of LSI is that it is based on light scattering, which is sensitive to many more parameters, and may thus be developed to become a truly versatile measurement technique.

Quantitative local velocity measurements that can noninvasively monitor (opaque) turbid media might be possible, because speckles are primarily sensitive to the transverse direction of motion, and the speckle contrast (among other speckle metrics) is sensitive to the magnitude of velocity [19,22]. When combined with regional laser Doppler techniques [20], which are sensitive to the longitudinal direction of motion, a three-dimensional flowmetry technique for turbid media might be developed. Light scattering is also sensitive to the refractive index of the red blood cells, which yields information about their oxygen content. LSI can also be used as a cheap technique for perfusion measurements [39]. Further possibilities include, but are not limited to, premature detection of atherosclerosis, measuring the dynamic morphology of red blood cells, and distinguishing between different depths in complex flow networks. The primary benefit of our new code is that we can enable or disable and vary parameters at will, allowing us to study their effect. For future work, our new code can thereby be used to study and develop said applications.

V. CONCLUSIONS

In this paper, we have developed and applied a computational model for simulating the interference of multiply scattered coherent light by moving particles. The model's purpose is to help us further develop laser speckle imaging (LSI) as a quantitative imaging technique. The model is based on Mie theory, which provides an exact solution for the scattering of a plane wave by a single sphere. The fields of all particles are gathered at the pixels of our simulated camera by adding them vectorially, and then squaring them to obtain the intensity. To incorporate multiple scattering, we devised an iterative process in which each particle scatters not only to every pixel, but also to every other particle. The process is repeated until successive scattering orders become negligible. Simplifying assumptions were made to make the process computationally feasible: we assumed that particles are sufficiently far apart (i.e., in each other's far field) and sufficiently small, so that they see scattered fields approximately as incoming plane waves. Although these assumptions affect the speckle pattern, they do not restrict us from obtaining meaningful results.

To show that our simplifications are not limiting, we have applied our model to a case study resembling blood flow: spherical particles of several micrometer moving in a cylindrical geometry with 1 m/s mean velocity. The flow system was modulated with a 1 Hz sinusoidal signal and a 1.20 Hz heartbeat signal. Using speckle blurring with a camera integration time of 100 μs, we have successfully retrieved the main frequency modes of the input signal from the speckles. We have studied the influence of speckle boiling on the quality of the result by comparing plug flow with a Poiseuille flow profile and found that speckle boiling applies uniform spectral noise to the signal. For our present case, its effect was of the same order as our measurement uncertainty, ∼2%, and thus speckle boiling was not found to be detrimental for the result. Our results prove that our numerical model is capable of simulating the whole LSI process and is therefore a useful tool for improving LSI as a quantitative indirect imaging technique.

[1] V. Tuchin, *Tissue Optics: Light Scattering Methods and Instruments for Medical Diagnosis* (SPIE Press, Bellingham, 2007).

[2] D. A. Boas, L. E. Campbell, and A. G. Yodh, Scattering and Imaging with Diffusing Temporal Field Correlations, Phys. Rev. Lett. **75**, 1855 (1995).

[3] M. A. O'Leary, D. A. Boas, B. Chance, and A. G. Yodh, Refraction of Diffuse Photon Density Waves, Phys. Rev. Lett. **69**, 2658 (1992).

[4] D. J. Pine, D. A. Weitz, P. M. Chaikin, and E. Herbolzheimer, Diffusing-Wave Spectroscopy, Phys. Rev. Lett. **60**, 1134 (1988).

[5] M. J. Stephen, Temporal fluctuations in wave propagation in random media, Phys. Rev. B **37**, 1 (1988).

[6] T. Durduran, R. Choe, W. B. Baker, and A. G. Yodh, Diffuse optics for tissue monitoring and tomography, Rep. Prog. Phys. **73**, 076701 (2010).

[7] A. J. Welch, M. J. C. van Gemert *et al.*, *Optical-Thermal Response of Laser-Irradiated Tissue*, Vol. 2 (Springer, New York, 2011).

[8] A. Sassaroli and F. Martelli, Equivalence of four Monte Carlo methods for photon migration in turbid media, JOSA A **29**, 2110 (2012).

[9] M. A. Davis and A. K. Dunn, Dynamic light scattering Monte Carlo: A method for simulating time-varying dynamics for ordered motion in heterogeneous media, Opt. Express **23**, 17145 (2015).

[10] N. Bosschaart, G. J. Edelman, M. C. G. Aalders, T. G. van Leeuwen, and D. J. Faber, A literature review and novel theoretical approach on the optical properties of whole blood, Lasers Med. Sci. **29**, 453 (2014).

[11] T. Asakura and N. Takai, Dynamic laser speckles and their application to velocity measurements of the diffuse object, Appl. Phys. **25**, 179 (1981).

[12] J. C. Dainty (Ed.), Laser speckle and related phenomena, in *Topics in Applied Physics*, Vol. 9 (Springer, Berlin, 1975).

[13] H. M. van der Kooij and J. Sprakel, Watching paint dry: More exciting than it seems, Soft Matter **11**, 6353 (2015).

[14] H. M. van der Kooij, R. Fokkink, J. van der Gucht, and J. Sprakel, Quantitative imaging of heterogeneous dynamics in drying and aging paints, Sci. Rep. **6**, 34383 (2016).

[15] D. A. Boas and A. K. Dunn, Laser speckle contrast imaging in biomedical optics, J. Biomed. Opt. **15**, 011109 (2010).

[16] P. Zakharov, A. C. Völker, M. T. Wyss, F. Haiss, N. Calcinaghi, C. Zunzunegui, A. Buck, F. Scheffold, and B. Weber, Dynamic laser speckle imaging of cerebral blood flow, Opt. Express **17**, 13904 (2009).

[17] M. Heckmeier, S. E. Skipetrov, G. Maret, and R. Maynard, Imaging of dynamic heterogeneities in multiple-scattering media, JOSA A **14**, 185 (1997).

[18] A. K. Dunn, Laser speckle contrast imaging of cerebral blood flow, Ann. Biomed. Eng. **40**, 367 (2012).

[19] D. D. Duncan and S. J. Kirkpatrick, Can laser speckle flowmetry be made a quantitative tool? J. Opt. Soc. Am. A **25**, 2088 (2008).

[20] D. Briers, D. D. Duncan, E. R. Hirst, S. J. Kirkpatrick, M. Larsson, W. Steenbergen, T. Stromberg, and O. B. Thompson, Laser speckle contrast imaging: Theoretical and practical limitations, J. Biomed. Opt. **18**, 066018 (2013).

[21] M. Nemati, G. B. Loozen, N. van der Wekken, G. van de Belt, H. P. Urbach, N. Bhattacharya, and S. Kenjeres, Application of full field optical studies for pulsatile flow in a carotid artery phantom, Biomed. Opt. Express **6**, 4037 (2015).

[22] A. F. Fercher and J. D. Briers, Flow visualization by means of single-exposure speckle photography, Opt. Commun. **37**, 326 (1981).

[23] J. D. Briers and S. Webster, Laser speckle contrast analysis (LASCA): A nonscanning, full-field technique for monitoring capillary blood flow, J. Biomed. Opt. **1**, 174 (1996).

[24] H. M. Pedersen, The roughness dependence of partially developed, monochromatic speckle patterns, Opt. Commun. **12**, 156 (1974).

[25] J. W. Goodman, Statistical properties of laser speckle patterns, in *Laser Speckle and Related Phenomena* (Springer, Berlin, 1975), pp. 9–75.

[26] J. Li, G. Yao, and L. V. Wang, Degree of polarization in laser speckles from turbid media: Implications in tissue optics, J. Biomed. Opt. **7**, 307 (2002).

[27] T. Yoshimura, Statistical properties of dynamic speckles, JOSA A **3**, 1032 (1986).

[28] R. Bandyopadhyay, A. S. Gittings, S. S. Suh, P. K. Dixon, and D. J. Durian, Speckle-visibility spectroscopy: A tool to study time-varying dynamics, Rev. Sci. Instrum. **76**, 093110 (2005).

[29] M. Nemati, S. Kenjeres, H. P. Urbach, and N. Bhattacharya, Fractality of pulsatile flow in speckle images, J. Appl. Phys. **119**, 174902 (2016).

[30] G. Mie, Beiträge zur Optik trüber Medien, speziell kolloidaler Metallösungen, Ann. Phys. **330**, 377 (1908).

[31] C. F. Bohren and D. R. Huffman, *Absorption and Scattering of Light by Small Particles* (John Wiley & Sons, Weimheim, 2008).

[32] J. A. Stratton, *Electromagnetic Theory* (John Wiley & Sons, Hoboken, New Jersey, 2007).

[33] H. C. Hulst, *Light Scattering by Small Particles* (Courier Corporation, New York, 1981).

[34] W. B. Baker, A. B. Parthasarathy, K. P. Gannon, V. C. Kavuri, D. R. Busch, K. Abramson, L. He, R. C. Mesquita, M. T. Mullen, J. A. Detre *et al.*, Noninvasive optical monitoring of critical closing pressure and arteriole compliance in human subjects, J. Cereb. Blood Flow Metab. **37**, 2691 (2017).

[35] S. E. Skipetrov, J. Peuser, R. Cerbino, P. Zakharov, B. Weber, and F. Scheffold, Noise in laser speckle correlation and imaging techniques, Opt. Express **18**, 14519 (2010).

[36] O. Thompson, M. Andrews, and E. Hirst, Correction for spatial averaging in laser speckle contrast analysis, Biomed. Opt. Express **2**, 1021 (2011).

[37] S. J. Kirkpatrick, D. D. Duncan, and E. M. Wells-Gray, Detrimental effects of speckle-pixel size matching in laser speckle contrast imaging, Opt. Lett. **33**, 2886 (2008).

[38] With our settings, 32 841 instantaneous optics simulations are performed for each simulation. Using 32 cores of a 2.4 GHz AMD Opteron 6234 processor, the simulation time for 256^2 pixels is 180 h. The runtime scales linearly with the number of pixels (so 512^2 pixels would take four times longer), and scales perfectly with the number of computing cores (so using merely one core would take 32 times longer).

[39] M. Draijer, E. Hondebrink, T. van Leeuwen, and W. Steenbergen, Review of laser speckle contrast techniques for visualizing tissue perfusion, Lasers Med. Sci. **24**, 639 (2009).

[40] W. J. Wiscombe, Improved Mie scattering algorithms, Appl. Opt. **19**, 1505 (1980).

[41] Y.-L. Xu and B. Å. S. Gustafson, A generalized multiparticle Mie-solution: Further experimental verification, J. Quant. Spectrosc. Radiat. Transfer **70**, 395 (2001).

[42] J. Markkanen and A. J. Yuffa, Fast superposition T-matrix solution for clusters with arbitrarily-shaped constituent particles, J. Quant. Spectrosc. Radiat. Transfer **189**, 181 (2017).

[43] We have previously applied our code to cases such as the double-slit experiment, in which we have found an exact match with theory for the distance between fringes.